Arabian Journal of Chemistry (2022) **15**, 103729

King Saud University

Arabian Journal of Chemistry

www.ksu.edu.sa
www.sciencedirect.com

ORIGINAL ARTICLE

Fabrication of an efficient ternary TiO_2/Bi_2WO_6 nanocomposite supported on g-C_3N_4 with enhanced visible-light- photocatalytic activity: Modeling and systematic optimization procedure

Hadiseh Mirhosseini [a,b], Ali Mostafavi [a,*], Tayebeh Shamspur [a], Ghasem Sargazi [c]

[a] *Department of Chemistry, Faculty of Science, Shahid Bahonar University of Kerman, Kerman, Iran*
[b] *Young Research Society, Shahid Bahonar University of Kerman, Kerman, Iran*
[c] *Noncommunicable Diseases Research Center, Bam University of Medical Science, Bam, Iran*

Received 17 November 2021; accepted 21 January 2022
Available online 28 January 2022

KEYWORDS

TiO_2/g-C_3N_4/Bi_2WO_6 nanocomposite;
New photocatalyst;
BG removal;
2^{k-1} factorial design;
Optimization design

Abstract In this study, a ternary TiO_2/g-C_3N_4/Bi_2WO_6 nanocomposite was prepared via a facial approach. The final structure was applied as a new photocatalyst for the removal of brilliant green (BG) dye, as a model of organic pollutants, from the aqueous solution. The results of FESEM, EDS with mapping, XRD, FTIR, UV–vis DRS, PL, and EIS analyses further demonstrate the successful establishment of heterojunction between TiO_2, g-C_3N_4, and Bi_2WO_6. Integration of g-C_3N_4 and Bi_2WO_6 with TiO2 was remarkably decreased the band gap energy of TiO_2 to 2.68 eV (from 3.15 eV). The effects of various experimental factors such as TiO_2/g-C_3N_4/Bi_2WO_6 dosage, initial BG concentration, visible irradiation time, and pH on the photocatalyst behavior of TiO_2/g-C_3N_4/Bi_2WO_6 were investigated by 2^{k-1} factorial design. The results of the analysis of variance demonstrate these experimental factors are effective on the BG degradation efficiency. The response surface methodology was applied to achieve the optimization procedure of BG degradation. According to these results, the complete BG removal efficiency was obtained for the optimal conditions of 15.76 mg of TiO_2/g-C_3N_4/Bi_2WO_6 nanocomposite, an initial BG concentration of 10 ppm, pH of 9, and time duration of 70 min. The improved photocatalytic performance of ternary TiO_2/g-C_3N_4/Bi_2WO_6 nanocomposite was related to the formation of heterojunction between TiO_2, g-C_3N_4, and Bi_2WO_6, significant light adsorption ability, and low recombination of photogenerated carriers.

1. Introduction

Environmental pollutions such as pesticides, pharmaceuticals, and dyes have become a global concern due to their effects on human health and aquatic life. Accordingly, the elimination

---

* Corresponding author.
E-mail address: amostafavi@uk.ac.ir (A. Mostafavi).

Peer review under responsibility of King Saud University.

Production and hosting by Elsevier

https://doi.org/10.1016/j.arabjc.2022.103729
1878-5352

and treatment of these pollutions have attracted intensive attention.

Brilliant green dye (BG) is a cationic dye, which has been widely applied in various applications such as paper, plastic, rubber, textiles industries as well as biological and chemical laboratories (Nithya et al., 2020). On the other hand, BG is a toxic compound that can be affected aquatic and human life (Khan et al., 2020). Therefore, improving an efficient, cost-effective, and environmentally friendly procedure for the removing of such dyes has become primary.

Compared to conventional methods such as coagulation (Zheng et al., 2020; Zhou et al., 2019), floatation (Shakir et al., 2010; Yuan et al., 2008), and membrane separation (Wang et al., 2019; Wang et al., 2020), advanced oxidation processes (AOPs) have aroused great interest in modern wastewater treatment (Eshaq et al., 2020; Maniakova et al., 2020; Muneer et al., 2021; Sun et al., 2020; Yu et al., 2013;). In AOPs, reactive oxygen species ($^{\cdot}OH$, H_2O_2, and $^{\cdot}O_2$) are formed, which are powerful oxidants and removed the pollutants through oxidation reaction (Baniamerian et al., 2020; Wang et al., 2014). AOPs have versatile characteristics, including high removal rate, short time, and high flexibility in design. Among the AOPs methods, semiconductor based photocatalysts are promising techniques for the removal of pollutants from water because of their ability to convert solar energy into chemical energy, mild working condition, low cost, and high efficiency (Zhang et al., 2022; Ahmadpour et al., 2020; Liu et al., 2021; Deng and Zhao, 2015).

Titanium dioxide (TiO_2) is an important semiconductor material, which has been intensively used as a photocatalyst in the wastewater treatment fields (Gao et al., 2020; Kovalevskiy et al., 2020; Lopes et al., 2020; Sharma et al., 2020). Nontoxicity, cost-effectiveness, photoactivity, and high stability are some of the unique properties, which have made TiO_2 one of the most promising photocatalyst materials (Abdel-Wahed et al., 2020; Chandra et al., 2016; Golshan et al., 2018). Nevertheless, the main problem in the application of pristine TiO_2 in the photocatalytic process is the wide band gap (3.2 eV approx.), which leads to its excitation only by ultraviolet (UV) light irradiation (Hafeez et al., 2019; Wei and Wang, 2018). Therefore, in order to improve photocatalytic performance, TiO_2 may be combined with other materials such as metal oxide (Li et al., 2020a,b,c; Tekin et al., 2020) and carbon nanomaterials (Huang et al., 2016; Noda et al., 2020).

Bismuth tungstate (Bi_2WO_6) is known as a promising photocatalyst in the field of environmental purification, because of its intriguing properties such as nontoxicity, physicochemical stability, wide solar response, and narrow band gap (Koutavarapu et al., 2020; Huang et al., 2019; Liu et al., 2020a,b; Yin et al., 2020; Yuan et al., 2020). However, the photocatalytic performance of Bi_2WO_6 is limited due to the quick recombination of photoexcited electrons and holes, which restrict its usage as the photocatalyst (Li et al., 2020a,b,c; Zhu and Zhou, 2020). One of the techniques for overcome to these limitations and increasing the separation efficiency is combination with other materials and designing heterojunction composite. Preparation of TiO_2/Bi_2WO_6 nanocomposite by coupling of TiO_2 with Bi_2WO_6 was improved absorption of visible light, the separation of electron-hole pairs and so the photocatalytic activity of the nanocomposite was enhanced (Shang et al., 2009).

Graphitic carbon nitride (g-C_3N_4) is a metal-free semiconductor, which has attracted intensive attention, owning to unique features such as tunable band gap, optical properties, non-toxic, cost-effective, and high thermal stability (Chinnapaiyan et al., 2020; Zhao et al., 2019). These significant properties lead to the application of g-C_3N_4 in the divers field such as sensor (Zhang et al., 2020; Guo et al., 2020; Ouyang et al., 2020), gas storage (Panigrahi et al., 2020) as well as photocatalysis phenomena (Karthik et al., 2020; Lakhera et al., 2020; Yang et al., 2020). Numerous studies have been reported on the use of g-C_3N_4 for removing contaminants via the photocatalytic procedure. However, g-C_3N_4 has some limitations such as small specific surface area, low conductivity, and fast recombination of electrons and holes, which restrict its usage as the photocatalyst (Li et al., 2020a,b,c; Zhao et al., 2019) . The combination of g-C_3N_4 with noble metals and other semiconductor materials is an efficient and simple process for improving the photocatalytic behavior of pristine g-C_3N_4. It seems that coupling g-C_3N_4 as a promising nanomaterial with TiO_2 and Bi_2WO_6 improve the photocatalytic efficiency. For instance Guo et al. was synthesized g-C_3N_4/Bi_2WO_6 heterojunction with great photocatalytic performance (Guo et al., 2018). The coupling of g-C_3N_4 and Bi_2WO_6 was decreased the recombination rate of photogenerated electron and hole pairs. Also, Kai et al. reported the synthesize TiO_2/g-C_3N_4 nanocomposite and displayed that both separation of electron-hole pairs and absorption of visible irradiation were improved (Kai et al., 2018).

TiO_2/g-C_3N_4/Bi_2WO_6 nanocomposite with an attractive photocatalytic activity could be expected due to low recombination of photoexcited carriers and its large specific surface area. Herein, we have reported the synthesis of TiO_2/g-C_3N_4/Bi_2WO_6 ternary heterojunction for effective photocatalytic removal of BG dye from aqueous solution. The morphology, particle size distribution, crystallographic properties, functional group, elemental composition, optical band gap, charge transfer properties, and charge separation performance of as-prepared TiO_2/g-C_3N_4/Bi_2WO_6 heterojunction have been analyzed by field emission scanning electron microscopy (FESEM), Energy dispersive X-ray spectroscopy (EDS), mapping, X-ray diffraction (XRD), Fourier transform infrared (FTIR), UV–Vis diffuse reflectance spectroscopy (DRS), photoluminescence (PL) spectroscopy, and Electrochemical impedance spectroscopy (EIS). Furthermore, a 2^{k-1} factorial design and a response surface methodology (RSM) was used to investigate the influences of key process factors on BG removal efficiency as well as optimizing the conditions for attaining the high BG removal efficiency. Finally, the synergetic photocatalytic mechanism of TiO_2/g-C_3N_4/Bi_2WO_6 ternary nanocomposite was proposed carefully in details based on the energy level diagram, which is a facile route for improving its photocatalytic activity. Such a ternary nanocomposite provides a promising approach to the elimination and treat of environmental pollutions.

2. Experimental

2.1. Materials and characterization

Titanium tetraisopropoxide (TTIP), isopropanol (C_3H_8O), nitric acid (HNO_3), melamine ($C_3H_6N_6$), methanol (CH_3OH), sodium tungstate dihydrate ($Na_2WO_4\cdot 2H_2O$), bismuth nitrate pentahydrate ($Bi(NO_3)_3\cdot 5H_2O$), cetyl trimethyl ammonium bromide (CTAB), ethanol (CH_3OH), sodium sulfate (Na_2SO_4) and brilliant green dye (BG, λ_{max}: 625 nm) were purchased from Sigma Aldrich and Merck companies and employed for the preparation of TiO_2, g-C_3N_4, Bi_2WO_6, and TiO_2/g-C_3N_4/Bi_2WO_6 nanocomposite.

FESEM, EDS, and mapping analyses were performed with a ZEISS SIGMA VP scanning electron microscope. The FT-IR spectra of samples were collected using a Tensor 27 spectrometer. X'pert PRO diffractometer under CuKα radiation (λ = 1.5406 °A) was applied to investigation the crystal structure of final products. Varian cry 50 spectrophotometer machine was also used to collect the UV–visible and diffuse reflectance spectra (DRS mode) of the products. The PL spectroscopy analysis of final products was carried out on the Cary Eclipse fluorescence spectrometer. The EIS data were collected by RADstat-10 through a standard three-electrode cell. In this system, a piece of Pt, Ag/AgCl electrode, glassy carbon electrode covered with the sample, and Na_2SO_4 (0.5 M) were applied as the counter electrode, reference electrode, working electrode, and electrolyte, respectively.

2.2. Synthesis of TiO_2 nanoparticles (NPs)

Hydrolyze, and peptization of TTIP solution method was used to synthesis of TiO_2 NPs (Hafeez et al., 2018).

In detail, isopropanol (15 mL) and TTIP solution (5 mL) was slowly dropped into 250 mL of DI water with pH ~ 3 (adjusted with HNO_3) under vigorous magnetic stirring. The mixing solution was stirred for another 3 h, and then heated at 70 °C in the oven for 22 h. The white product was collected with the help of centrifugation and washed with DI water before drying at 70 °C. Finally, the obtained product was calcinated at 400 °C for 2 h.

2.3. Synthesis of g-C_3N_4 nanosheets

The bulk g-C_3N_4 was prepared via one step polymerization of melamine (Vadivel et al., 2016). In a typical procedure, a certain amount of melamine was heated in a tube furnace at 550 °C for 4 h with a ramp rate of 10 °C min^{-1} under air atmosphere. Then, to synthesis g-C_3N_4 nanosheet, the yellow-colored bulk g-C_3N_4 was grounded to powder and treated with ultrasound in methanol (30 min). The as-prepared products were washed repeatedly with DI water and dried at 70 °C (Ding et al., 2015).

2.4. Synthesis of Bi_2WO_6 nanosheets

Bi_2WO_6 nanosheets were synthesized via hydrothermal procedure (Wu et al., 2020). Typically, 2 mmol $Bi(NO_3)_3\cdot 5H_2O$ was dissolved in 80 mL of DI water with the aid of ultrasonication for 15 min. Then, 1 mmol $Na_2WO_4\cdot 2H_2O$ and 50 mg CTAB were slowly added to the resultant solution under vigorous magnetic stirring, and this mixture was stirred for another 30 min. The resulting mixture was moved into a 100 mL Teflon-lined stainless autoclave and was heated at 120 °C for 24 h. The final precipitates were centrifuged, washed repeatedly with DI water, and dried at 60 °C.

2.5. Synthesis of TiO_2/g-C_3N_4/Bi_2WO_6 nanocomposite

100 mg of each TiO_2, g-C_3N_4, and Bi_2WO_6 were dispersed separately in 30 mL of ethanol. Then, three solutions were mixed together, and magnetically stirred at 50 °C for 24 h. The nanocomposite was isolated by centrifugation and dried at 60 °C overnight.

2.6. Photocatalytic activity studies

The photocatalytic performance of TiO_2/g-C_3N_4/Bi_2WO_6 nanocomposite was tested via removal of BG dye under visible light irradiation. Typically, a certain amount of photocatalyst was dispersed in 10 mL of BG dye aqueous solution. Then, the mixture was stirred in the dark to establish adsorption/desorption equilibrium. After that, the resultant mixture was irradiated using 50 W LED lamp under continuous stirring. After a specific visible irradiation time, the content of BG dye was tested by a UV–Vis spectrophotometer at 625 nm.

2.7. Experimental design

The photocatalytic degradation procedure was optimized via 2^{k-1} factorial design. In other words, the 2^{k-1} factorial design was applied for the investigation of the factors affecting the degradation efficiency of BG dye. The selected factors in this study were catalyst dosage (A), initial BG dye concentration (B), irradiation time (C), and pH (D) as the variables and removal % as the response. Each variable factors was evaluated at three levels (-1, 0, +1) (Table 1). The experimental design and responses for two replicates are presented in Table 2.

3. Results and discussion

3.1. Morphological and elemental study

FE-SEM analysis was applied to investigate the surface morphology of TiO_2 and Bi_2WO_6, as well as TiO_2/ g-C_3N_4/ Bi_2WO_6 nanocomposite and the images presented in Fig. 1a. As shown in Figure, the pristine TiO_2 and Bi_2WO_6 show spherical and nanosheet structure, respectively. The FESEM image of as-prepared TiO_2/ g-C_3N_4/ Bi_2WO_6 nanocomposite includes TiO_2 nanoparticles and Bi_2WO_6 nanosheets as well as g-C_3N_4 nanosheets, which can be confirmed the successful synthesis of the nanocomposite. Also, TiO_2 nanoparticles and Bi_2WO_6 nanosheets are well dispersed on the surface of g-C_3N_4 nanosheets. The purity of the TiO_2/g-C_3N_4/Bi_2WO_6 heterojunction was evaluated via EDS analysis (Fig. 1b). The results revealed that the nanocomposite consists of C, N, Ti, Bi, O, and W elements. Also, elemental mapping analysis showed the homogeneous distribution of C, N, Ti, Bi, O, and W elements on the final nanocomposite (Fig. 1c). The EDS and elemental mapping analysis further confirm the hybridization of TiO_2, g-C_3N_4, and Bi_2WO_6.

3.2. XRD characterization

Fig. 2a shows the XRD patterns of TiO_2, g-C_3N_4, Bi_2WO_6, and TiO_2/g-C_3N_4/Bi_2WO_6 nanocomposite. According to the

Table 1 Coded and uncoded levels for 2 $^{k-1}$ factorial design of effective parameter on the photodegradation behavior of TiO_2/g-C_3N_4/Bi_2WO_6 nanocomposite.

Level	Coded level	Uncoded level			
		Catalyst dosage (mg)	BG concentration(ppm)	Contact time(min)	pH
High	+1	20	20	70	9
Center	0	15	15	50	6
Low	−1	10	10	30	4
Coded formula : $\frac{x-\frac{x(high)+x(low)}{2}}{\frac{x(high)-x(low)}{2}}$, x: -ω …, −3, −2, −1, 0, 1, 2, 3, .. + ω					

XRD pattern of TiO_2, the diffraction peaks at 25.55, 37.94, 48.28, 55.0, 63.10, 70.02, 75.6° are assigned to the (101), (004), (200), (211), (204), (220), (215) plans, respectively, which are agree with its anatase phase (JCPDS 00–021-1272) (Hafeez et al., 2018).Also, the XRD pattern of g-C_3N_4 nanosheets was shown two diffraction peaks at 27.72 and 13.07, which can be corresponded to reflections of (002) and (100) plans (Ding et al., 2015) .Besides, the XRD pattern of pristine Bi_2WO_6 shown diffraction peaks at 10.59°, 28.49°, 31.59°, 33.46°, 35.12°, 36.88°, 39.70°, 42.40°, 46.54°, 47.94°, 49.03°, 55.07°, 56.12°, 58.41°, and 59.28° related to (020), (131), (060), (002), (151), (112), (042), (152), (241), (152), (202), (222), (262), (133), (262), and (351) plans, respectively, which can be corresponded to the orthorhombic crystal phase of Bi_2WO_6 (JCPDS 00–039-0256) (Liu et al., 2020a,b). The XRD pattern of TiO_2/g-C_3N_4/Bi_2WO_6 heterojunction demonstrates the presence of TiO_2, g-C_3N_4, and Bi_2WO_6 in the ternary nanocomposite. Therefore, this Figure is shown that the crystal phase of TiO_2, g-C_3N_4, and Bi_2WO_6 were not changed and the formation of ternary nanocomposite was confirmed.

3.3. FT-IR analysis

The FT-IR spectra of TiO_2, g-C_3N_4, Bi_2WO_6, and TiO_2/g-C_3N_4/Bi_2WO_6 nanocomposite are depicted in Fig. 2b. For pristine TiO_2, the absorption bands at the range of 500–800 cm^{-1} are assigned to Ti-O and Ti-O-Ti stretching vibration. The peaks around 1635 cm^{-1} and 3450 cm^{-1} are related to Ti-OH bending bands and O-H stretching bands, respectively (Hafeez et al., 2018; Hafeez et al., 2019). According to the FT-IR spectrum of pure g-C_3N_4 nanosheet, the peak at 807 cm^{-1} is ascribed to absorption of tri-s-triazine units. The absorption bands located at 1236 cm^{-1}, 1317 cm^{-1}, 1405 cm^{-1}, and 1571 cm^{-1} are related to C-N aromatic stretching vibration, while the peak around 1637 cm^{-1} is corresponded to stretching vibration of C = N. In addition, the broad band at 3000–3500 cm^{-1} were assigned to stretching vibration of OH, NH, and NH_2 groups (Chinnapaiyan et al., 2020; Raza et al., 2018) .For pure Bi_2WO_6, the absorption peaks at 500–1000 cm^{-1} were related to O-W-O, W-O, and Bi-O stretching vibration (Liu et al., 2020a,b). The FT-IR spectrum of TiO_2/g-C_3N_4/Bi_2WO_6 nanocomposite contains

Table 2 Randomized complete 2 $^{K-1}$ factorial design for BG degradation experiments by TiO_2/g-C_3N_4/Bi_2WO_6 nanocomposite.

Sample (Level)	Std Order	Run Order	Center Pt	Blocks	A (mg)	B (ppm)	C (min)	D	REP	Removal (%)
a	4	1	1	1	+1	+1	−1	−1	1	86.53
									2	84.12
b	10	2	1	1	+1	−1	−1	+1	1	93.5
									2	93.01
c	3	3	1	1	−1	+1	−1	+1	1	68.81
									2	69.02
d	7	4	1	1	−1	+1	+1	−1	1	65.23
									2	66.17
e	6	5	1	1	+1	−1	+1	−1	1	95.11
									2	95.38
f	1	6	1	1	−1	−1	−1	−1	1	65.23
									2	65.52
g	18	7	0	1	0	0	0	0	1	90.66
									2	91.06
h	5	9	1	1	−1	−1	+1	−1	1	87.06
									2	88.12
i	8	12	1	1	+1	+1	+1	+1	1	83.31
									2	84.05

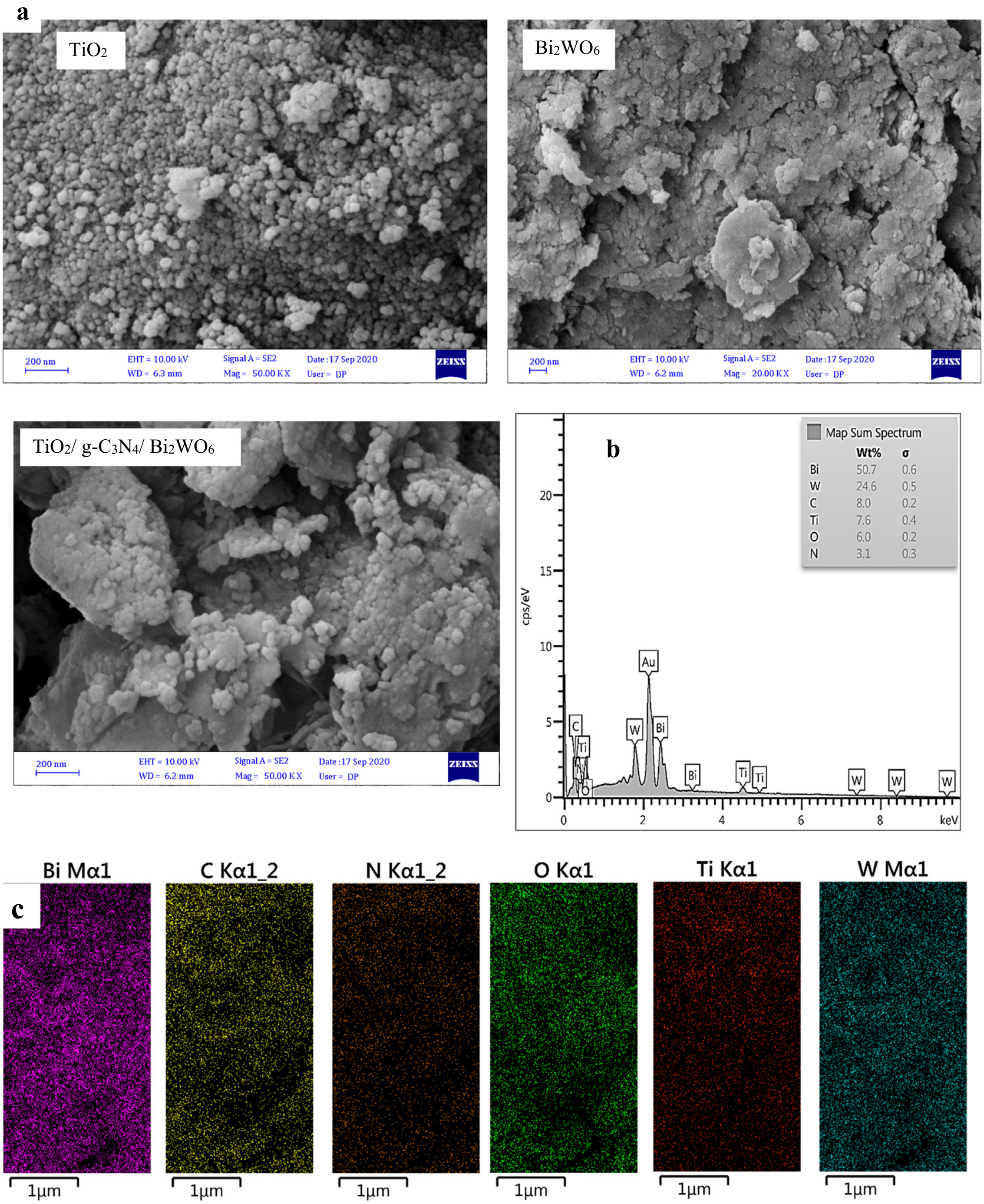

Fig. 1 FE-SEM image TiO_2, Bi_2WO_6, and TiO_2/g-C_3N_4/Bi_2WO_6 nanocomposite (a), EDS spectrum (b), and elemental mapping (c) of TiO_2/g-C_3N_4/Bi_2WO_6 nanocomposite.

the characteristic peaks of TiO_2, g-C_3N_4, Bi_2WO_6, which confirm the successful synthesis of heterojunction.

3.4. UV–Vis DRS spectra

The optical properties of TiO_2, g-C_3N_4, Bi_2WO_6, and TiO_2/g-C_3N_4/Bi_2WO_6 nanocomposite were investigated via UV–Vis DRS spectroscopy, and the spectra were depicted in Fig. 3a. Also, the band gap energies (E_g) of final products were measured on the basis of $\alpha h\nu = A(h\nu - E_g)$ Equation and plotting $(\alpha h\nu)^2$ vs. $h\nu$ (Fig. 3b) (Liu et al., 2020a,b; Zhang et al., 2018). Where, α is the absorption coefficient, h indicates the Planck's constant, ν denotes the frequency of the light, E_g represents the band gap energy, and A denotes a constant. As can be seen, the respective band gap energies of pure TiO_2, g-C_3N_4, Bi_2WO_6, and TiO_2/g-C_3N_4/Bi_2WO_6 heterojunction were estimated to be 3.15 eV, 2.68 eV, 2.96 eV, and 2.71 eV, respectively. Compared to the single TiO_2, the heterojunction exhibited the red shift and reduction in the band gap energy. It is found from the results that g-C_3N_4 and Bi_2WO_6 modifica-

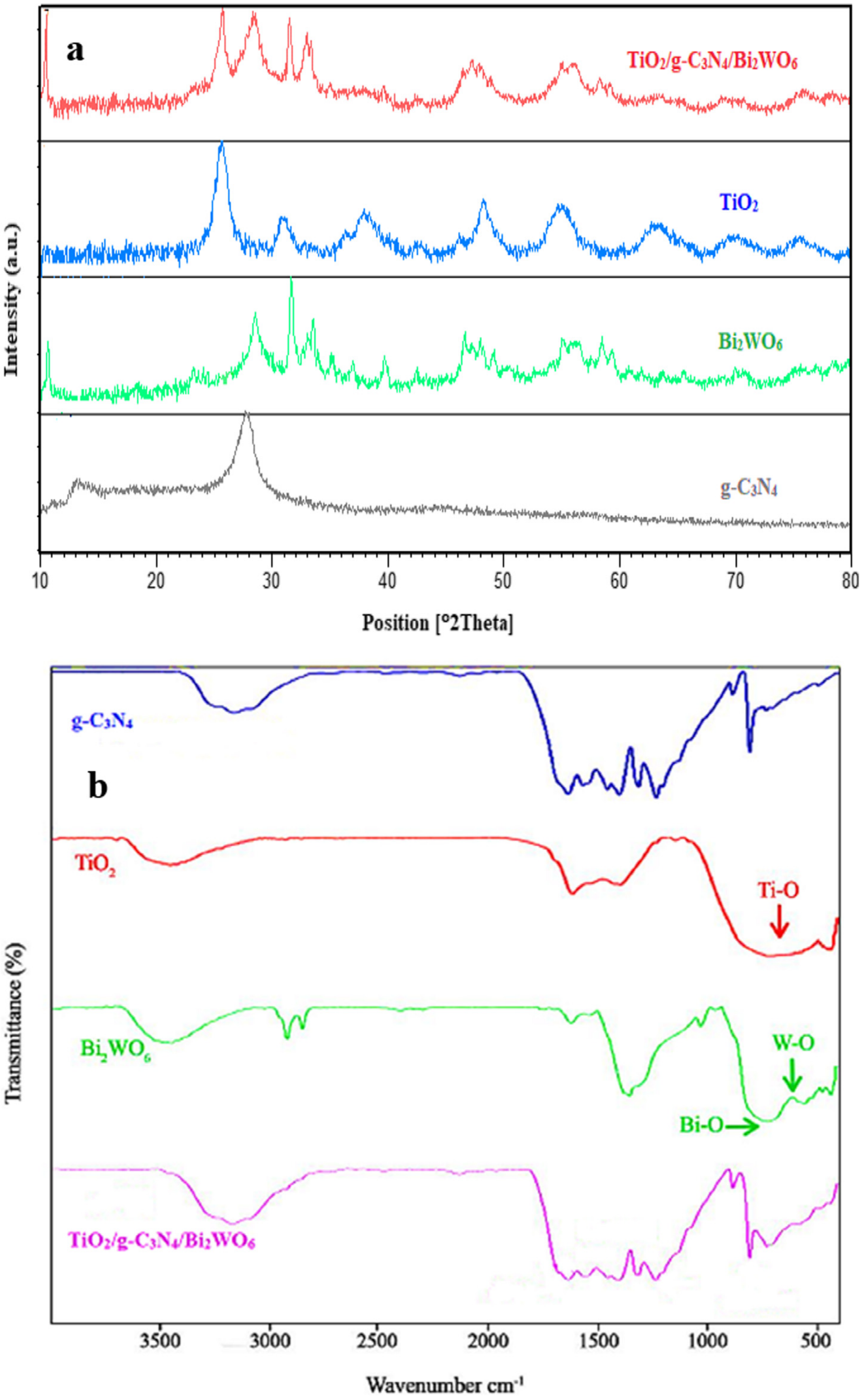

Fig. 2 XRD patterns (a), and FTIR spectra of TiO_2, g-C_3N_4, Bi_2WO_6, and TiO_2/g-C_3N_4/Bi_2WO_6 nanocomposite.

tion improve the optical properties of TiO_2 and enhance the visible light absorption.

3.5. Photoluminescence (PL) spectra

The PL emission was created by recombination of photoinduced electron and hole pairs (Raza et al., 2018). The PL emission peak intensity is in proportion to the rate of electron and hole pairs recombination. So, the PL analysis was applied to study the electron and hole separation performance of TiO_2, g-C_3N_4, Bi_2WO_6, and TiO_2/g-C_3N_4/Bi_2WO_6 nanocomposite, and the spectra were presented in Fig. 3c. According to the results, the pristine g-C_3N_4 and Bi_2WO_6 show high PL emissions, which indicated the high photogenerated carriers recom-

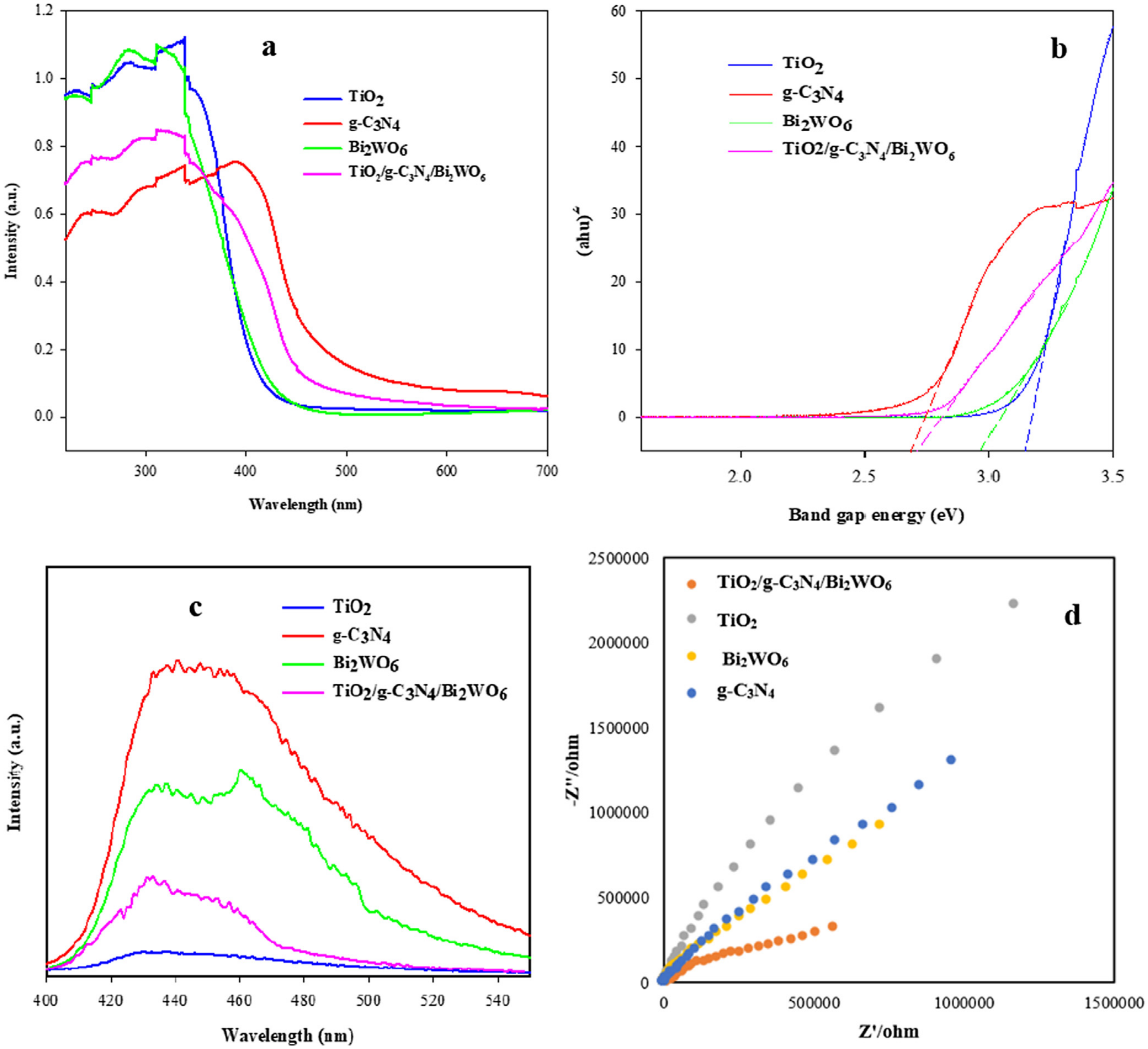

Fig. 3 Diffuse reflectance spectra (a), Tauc's plots (b), PL spectra (c), and EIS Nyquist plots (d) of TiO_2, $g\text{-}C_3N_4$, Bi_2WO_6, and $TiO_2/g\text{-}C_3N_4/Bi_2WO_6$ nanocomposite.

bination rate in bare $g\text{-}C_3N_4$ and Bi_2WO_6. After incorporating the Bi_2WO_6 and TiO_2 into the $g\text{-}C_3N_4$, the PL emission intensity of $TiO_2/g\text{-}C_3N_4/Bi_2WO_6$ nanocomposite was decreased because of the low electron and hole recombination rate in the heterostructure. These results can confirm the significant ability of nanocomposite in the charge separation and excellent photocatalytic activity.

3.6. Electrochemical impedance spectroscopy (EIS)

The electron transfer performance and interfacial properties of TiO_2, $g\text{-}C_3N_4$, Bi_2WO_6, and $TiO_2/g\text{-}C_3N_4/Bi_2WO_6$ nanocomposite were analyzed by electrochemical impedance spectroscopy (Fig. 3d). The semicircle arc diameter of EIS spectra represent the interface layer resistance of photoelectrodes (Chang et al., 2020). The larger semicircle diameter of EIS Nyquist plots indicates a lower charge transfer (Li et al., 2020a,b,c). The EIS Nyquist plots of final products were presented in Fig. 3d. The radius of the semicircle arc of $TiO_2/g\text{-}C_3N_4/Bi_2WO_6$ heterojunction is smaller than other samples, which indicates that the fast charge transfer and improvement in the photocatalytic performance.

3.7. Systematic study

3.7.1. 2^{k-1} fractional design

According to the bath experiments, the catalyst dosage, irradiation time, initial BG concentration, and pH were selected as four key factors affecting the degradation efficiency of BG by $TiO_2/g\text{-}C_3N_4/Bi_2WO_6$ nanocomposite. The 2^{k-1} fractional

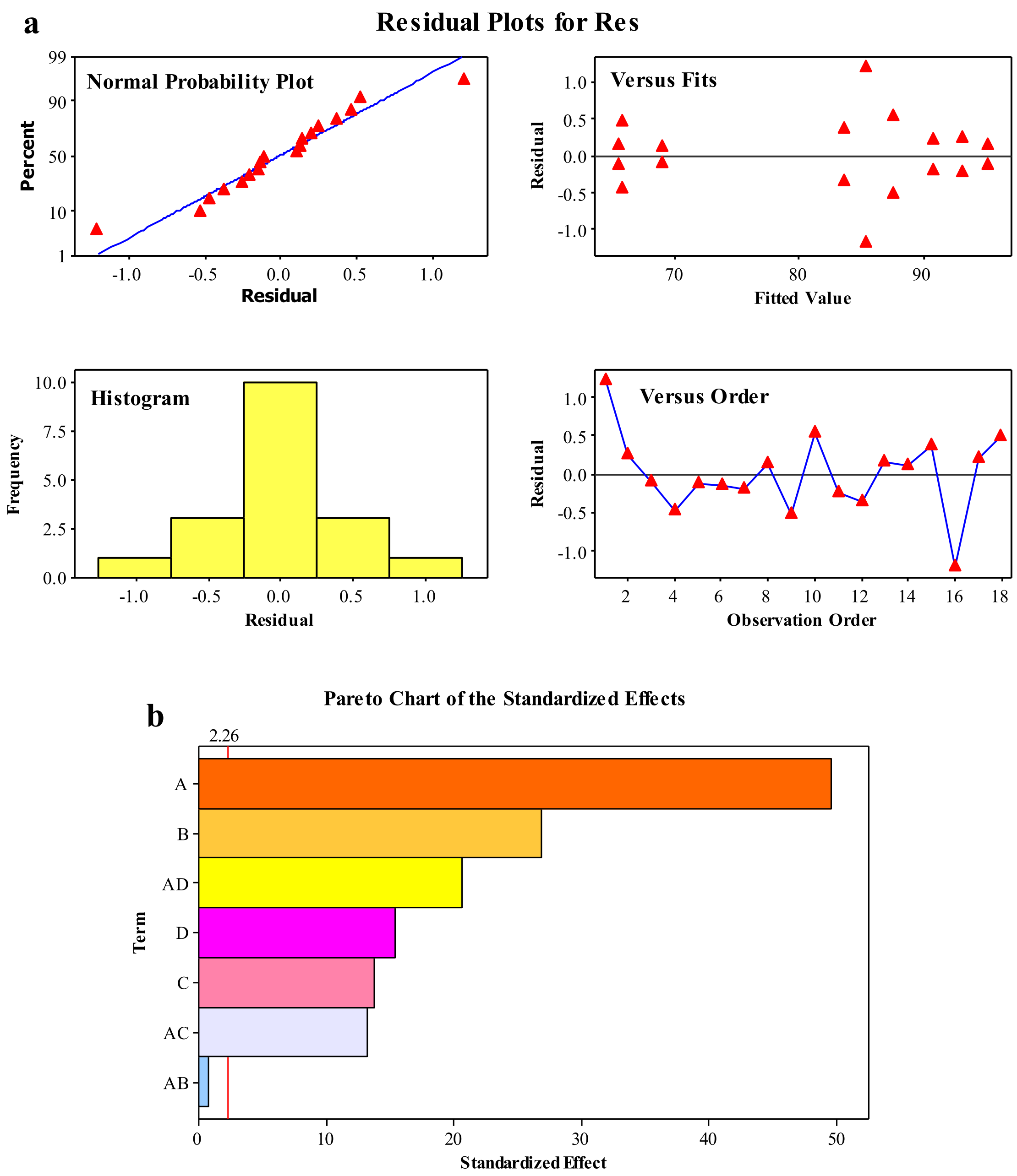

Fig. 4 Normal probability plots of the residuals for photodegradation behavior of TiO_2/g-C_3N_4/Bi_2WO_6 nanocomposite (a), and pareto charts of the experimental parameters effects on photodegradation performance of TiO_2/g-C_3N_4/Bi_2WO_6 nanocomposite (b).

analysis was used to optimize the key parameters for attaining high BG degradation efficiency. Table 2 represents the experimental design and related response data for two replicates experiments. Also, the residual diagrams for degradation efficiency of nanocomposite in various modes of normal probability, versus fit, histogram, and versus order were presented in Fig. 4a. As can be seen, TiO_2/g-C_3N_4/Bi_2WO_6 ternary nanocomposite has a randomized dispersion, exhibited the scientific distribution of each experiment.

3.7.2. *Anova*

Analysis of variance (ANOVA) was performed to evaluate the suggested model adequacy and also investigate the influence of experimental factors on the photocatalytic activity of TiO_2/g-C3N4/Bi_2WO_6 heterojunction (Table 3). In this method, if p_{value} was less than α_{value} = 0.050, the factor would affect the response amount of removal at 95% confidence level. According to the results, the p_{value} for the parameters of A, B, C, D, and E was 0.000, and therefore, these parameters had significant effects on the BG removal. As present in Table 3, the model with the F_{value} of 899.96 and the P_{value} of 0.000 verified the significant effects of this model. Also, the predicted-R^2 of 0.9921 is in agreement with the adjusted-R^2 of 0.9963 that suggests good significance and predictability of the model. According to the data attained from $2^{\ k-1}$ fractional and ANOVA methods, the relationship between exper-

Table 3 Analysis of Variance for BG degradation experiments using $TiO_2/g\text{-}C_3N_4/Bi_2WO_6$ nanocomposite.

Source	DF	Seq SS	Adj SS	Adj MS	F_{value}	P_{value}
Model	4	1792.75	1792.75	448.19	899.96	0.000
A	1	1222.38	1222.38	1222.38	2454.54	0.000
B	1	358.66	358.66	358.66	718.99	0.000
C	1	93.56	93.56	93.56	187.86	0.000
D	1	118.76	118.76	118.76	238.46	0.000
2-way Interactions	3	298.52	298.52	298.52	199.81	0.000
A*B	1	0.33	0.33	0.33	0.66	0.438
A*C	1	87.00	87.00	87.00	174.70	0.000
A*D	1	211.19	211.19	211.19	424.08	0.000
Curvature	1	185.85	185.85	185.85	373.18	0.000
Residual Error	9	4.48	4.48	0.50	1.03	0.325
Pure Error	9	4.48	4.48	0.50	0.57	0.462
Total	17	2281.60	2281.60	29.29	15.81	0.000
Lack-of-Fit	4		484.37	121.09	243.15	0.000

R-Sq = 99.80%, R-Sq (pred) = 99.21%, R-Sq (adj) = 99.63%

imental factors and response (removal %) was obtained by the regression equation, which is presented in the following equation:

$$Removal(\%) = 81.8 + 8.74A - 4.73B + 2.42C + 2.72D \tag{1}$$

The Pareto diagram shows the significant contribution of experimental factors on BG degradation percentage (Fig. 4b). This diagram is in line with ANOVA results, which verify the significant effects of the factors on the response (A, B, C, D, and E).

3.7.3. Response surface graph

RSM was utilized to determine the impact of each factor considering all interactions between factors in the 2 $^{k-1}$ fractional and also to optimize the degradation efficiency. So, three-dimensional surface plots were prepared for the prediction responses (Fig. 5). In each surface plot, two operating factors were changed and another factors were held constant. Using the surface plots, the efficiency for various values of the applied factors can be predicted. According to the results, with enhancement in the photocatalyst dosage, the photodegradation of BG was increased. Clearly, enhancement in the amount of photocatalyst provided more active sites, and as a result, the values of hydroxyl radicals were increased. A further enhancement in the photocatalyst dosage leads to a diminishing in the removal of BG, which can be related to the decrease in the active sites because of aggregation of photocatalyst particles. Also, the BG degradation efficiency was reduced with the rise in the concentration of BG. It can be attributed to the increase in the number of dye molecules and enhancement in the competition of these molecules for vacant sites. Also, a rise in the amount of dye molecules lead to less light passes through the solution. As can be seen, increasing in the time leads to enhance in the dye removal. When the contact time exceeds a certain limit, the degradation of dye reaches constant due to the saturation of the surface photocatalyst. With the rise in the pH solution, the degradation of BG was increased due to enhancement in the amount of OH free radicals. Overall, the suggested optimal conditions by RSM (Fig. 6) for the four experimental factors of the catalyst dosage, initial BG concentration, irradiation time, and pH were found to be 15.76 mg, 10 ppm, 70 min, and 9, respectively (Table 4). In these optimized conditions, the degradation percentage was estimated 100 %. Under these optimized conditions the experimental values for degradation percentage of BG was obtained 99.92 %. These results indicate the proper matching between predicted and experimental results.

3.8. Photocatalytic evaluation

The photodegradation of BG by $TiO_2/g\text{-}C_3N_4/Bi_2WO_6$ nanocomposite was compared with pristine TiO_2, $g\text{-}C_3N_4$, and Bi_2WO_6 nanostructures in the same operational conditions, and the results were presented in Fig. 7a. According to the results, the photocatalytic performance of $TiO_2/g\text{-}C_3N_4/Bi_2WO_6$ nanocomposite is better than those of TiO_2, $g\text{-}C_3N_4$, and Bi_2WO_6 nanostructures. The low amount of BG degradation for pure TiO_2 is due to the wide band gap energy (3.15 eV) and thus could not be excited by visible light irradiation. Also, the low photodegradation of $g\text{-}C_3N_4$, and Bi_2WO_6 indicating the fast recombination of photoexcited electrons and holes. However, the photocatalytic performance was increased with the combination of TiO_2, $g\text{-}C_3N_4$, and Bi_2WO_6 and formation $TiO_2/g\text{-}C_3N_4/Bi_2WO_6$ heterostructure because of synergistic interactions between TiO_2, $g\text{-}C_3N_4$, and Bi_2WO_6.

3.9. Kinetic study

Pseudo-first-order kinetic model was applied to investigate the kinetic of BG degradation reaction by $TiO_2/g\text{-}C_3N_4/Bi_2WO_6$ nanocomposite (Fig. 7b) as follows:

$$ln(C0/C) = k_{app}t \tag{2}$$

Where C_0 (mg.L^{-1}) is the initial concentration of BG, C (mg.L^{-1}) is the concentration of BG in any time t, k_{app} (min^{-1}) indicates the rate constant of BG degradation, and t (min) is the irradiation time. As can be seen in Figure, the k_{app} and R^2 values for $TiO_2/g\text{-}C_3N_4/Bi_2WO_6$ heterostructure are 0.097 min^{-1} and 0.983, respectively, which confirm the BG degradation was well explained by the pseudo-first-order kinetic model.

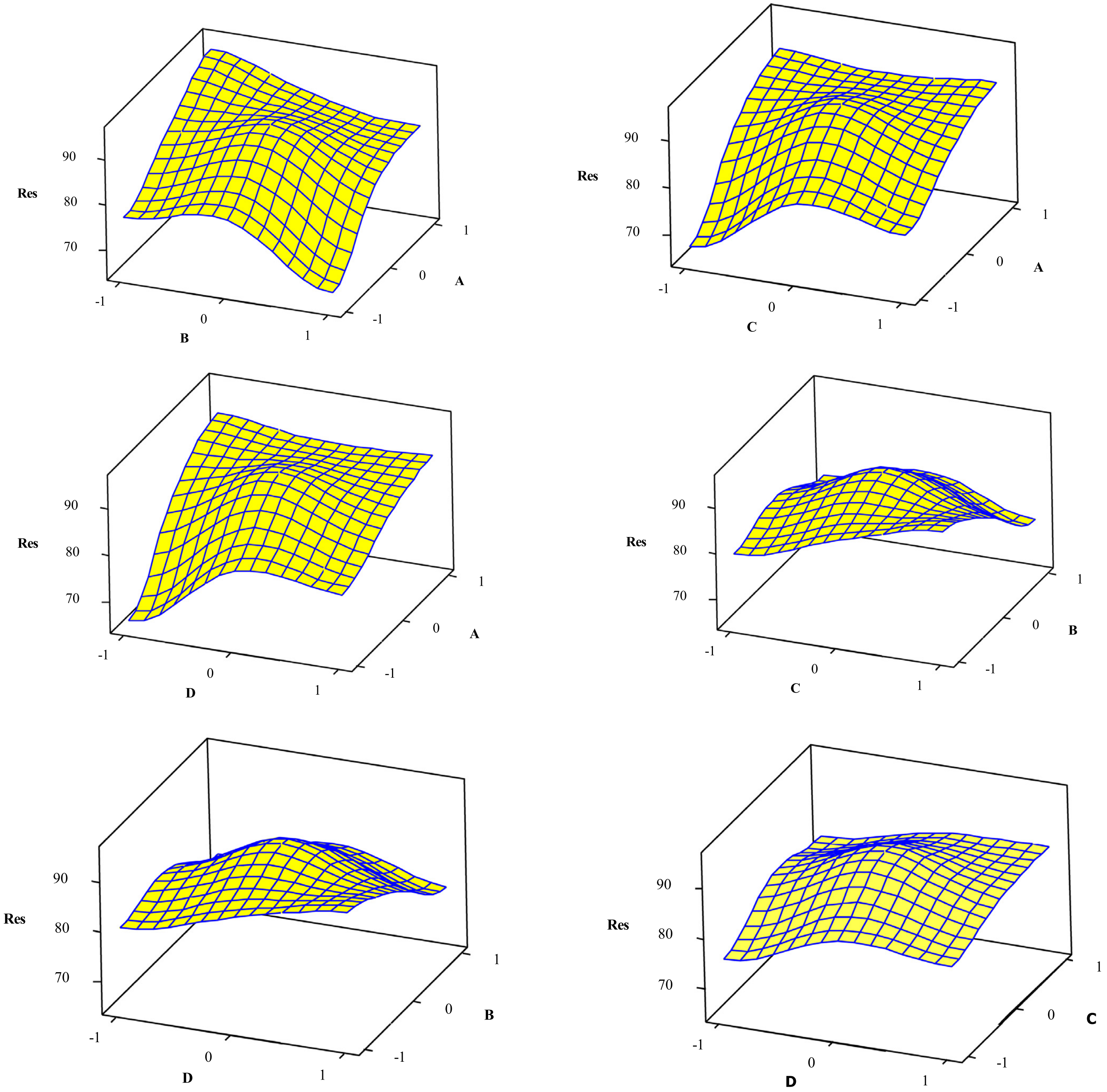

Fig. 5 Surface plots for BG degradation obtained from a regression model by $TiO_2/g\text{-}C_3N_4/Bi_2WO_6$ nanocomposite.

3.10. Stability of $TiO_2/g\text{-}C_3N_4/Bi_2WO_6$nanocomposite

Investigation of the photocatalysts stability is an important issue for their practical and large-scale utilization. So, the stability of $TiO_2/g\text{-}C_3N_4/Bi_2WO_6$ nanocomposite was tested by application of used photocatalyst for six times, and the results were shown in Fig. 7c. Before each cycle, the $TiO_2/g\text{-}C_3N_4/Bi_2WO_6$ photocatalyst was washed with DI water and ethanol solution, and dried at 60 °C. According to the results, the degradation efficiency of $TiO_2/g\text{-}C_3N_4/Bi_2WO_6$ nanocomposite showed no significant decrease in the performance of nanocomposite after six runs. This behavior confirmed the good stability and recyclability of $TiO_2/g\text{-}C_3N_4/Bi_2WO_6$ photocatalyst.

3.11. Proposed mechanism

The band edge potential of $TiO_2/g\text{-}C_3N_4/Bi_2WO_6$ nanocomposite is an important factor in the migration direction of electron and hole pairs. For a semiconductor, the conduction band (CB) and valance band (VB) potentials could be calculated theoretically as follows:

$$E_{VB} = c - E_e + 0.5E_g \quad (3)$$

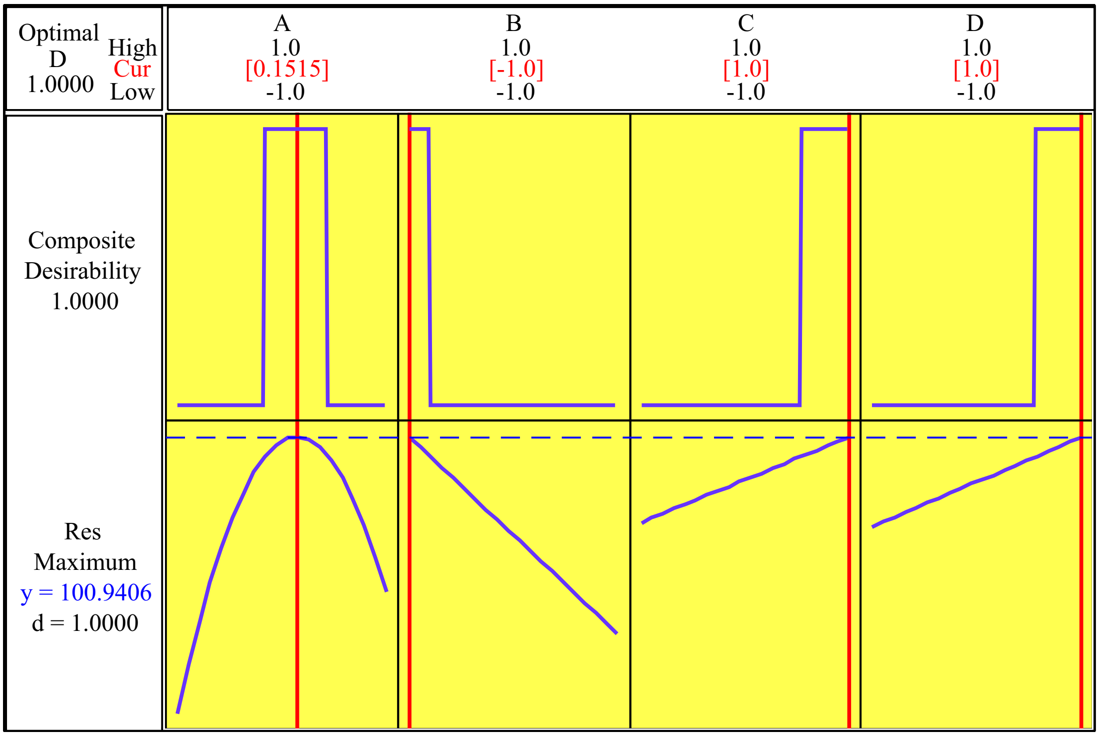

Fig. 6 Optimization RSM plots for BG degradation by $TiO_2/g\text{-}C_3N_4/Bi_2WO_6$ nanocomposite.

$$E_{CB} = E_{VB} - E_g \quad (4)$$

Where E_{VB} and E_{CB} indicate the VB and CB edge potentials, respectively, χ exhibited the geometric mean of the electronegativity of the constituent atoms, E_e denotes the energy of free electrons on the hydrogen scale (~4.5 eV), and E_g is related to the band gap energy of semiconductor (Tiana et al., 2015; Hafeez et al., 2018). Based on the UV–Vis DRS spectra (Fig. 3b), the E_g values of TiO_2, $g\text{-}C_3N_4$, and Bi_2WO_6 were found to be 3.15 eV, 2.68 eV, and 2.96 eV, respectively. The positions of VB and CB of TiO_2, $g\text{-}C_3N_4$, and Bi_2WO_6 were calculated via equations (3) and (4), respectively. The results were presented in Table 5. Based on the above results, the energy level diagram and possible charge-transfer mechanism of the $TiO_2/g\text{-}C_3N_4/Bi_2WO_6$ ternary heterojunction was proposed and depicted in Fig. 8. Under visible light irradiation, the electrons were excited in $g\text{-}C_3N_4$, and Bi_2WO_6 so, their CBs and VBs were repositioned the electron-rich and hole-rich, respectively. Normally, electrons and holes are quickly recombined in individual $g\text{-}C_3N_4$, and Bi_2WO_6. However, TiO_2 cannot excited by visible light irradiation because of the wide band gap energy therefore, the photogenic carriers are impossible to form (Huang et al., 2016). The E_{CB} value of $g\text{-}C_3N_4$ (-1.17 eV) is more negative than that of TiO_2 (-0.265 eV) therefore, the electrons in the $g\text{-}C_3N_4$ CB transfer to TiO_2 CB. Also, the electrons on the TiO_2 CB transfer to Bi_2WO_6 CB because the E_{CB} (-0.256 eV) position of TiO_2 is negative than that of Bi_2WO_6 (0.38 eV). Based on the energy level diagram, the photo-excited electrons at the CB of $g\text{-}C_3N_4$ can easily transfer to the Bi_2WO_6 CB through the TiO_2 CB. The E_{CB} of Bi_2WO_6 (0.38 eV) is positive than standard redox potential of $O_2/{}^{\cdot}O_2^-$ (-0.33 eV), signifying that the electrons in the CB of Bi_2WO_6 unable to reduce O_2 to ${}^{\cdot}O_2^-$. Meanwhile, the E_{VB} of $g\text{-}C_3N_4$ (1.51 eV) is more negative than the others, therefore the holes can be stayed on the $g\text{-}C_3N_4$ VB. The standard redox potentials of $OH^-/{}^{\cdot}OH$ (1.99 eV) and $H_2O/{}^{\cdot}OH$ (2.37 eV) are positive than the potential of $g\text{-}C_3N_4$ VB (1.51 eV), suggesting that the holes on the $g\text{-}C_3N_4$ VB are unable to react with H_2O and OH^- molecules to produce ${}^{\cdot}OH$ free radicals (Chen et al., 2019; Huang et al., 2016). Thereby, the holes remain on the $g\text{-}C_3N_4$ VB and oxidize the organic pollutants directly (Huang et al., 2016). On the other hand, the standard redox potentials of O_2/H_2O_2 (0.685 eV) is positive than E_{CB} of Bi_2WO_6 (0.38 eV), showing that the electrons in the Bi_2WO_6 CB can react with the O_2 and H^+ to generate H_2O_2, then the H_2O_2 species combine with electron to produce active species ${}^{\cdot}OH$. Hence, the formation of heterojunction between TiO_2, $g\text{-}C_3N_4$, and Bi_2WO_6 effectively improved the photo-excited electrons and holes separation,

Table 4 Response optimization for removal experimental parameters obtained from RSM (uncoded).

Response	Goal	Lower	Target	Upper	Parameter				Predict response value
					A (mg)	B (min)	C (ppm)	D	
%Removal	maximum	1	100	100	15.76	70	10	9	100

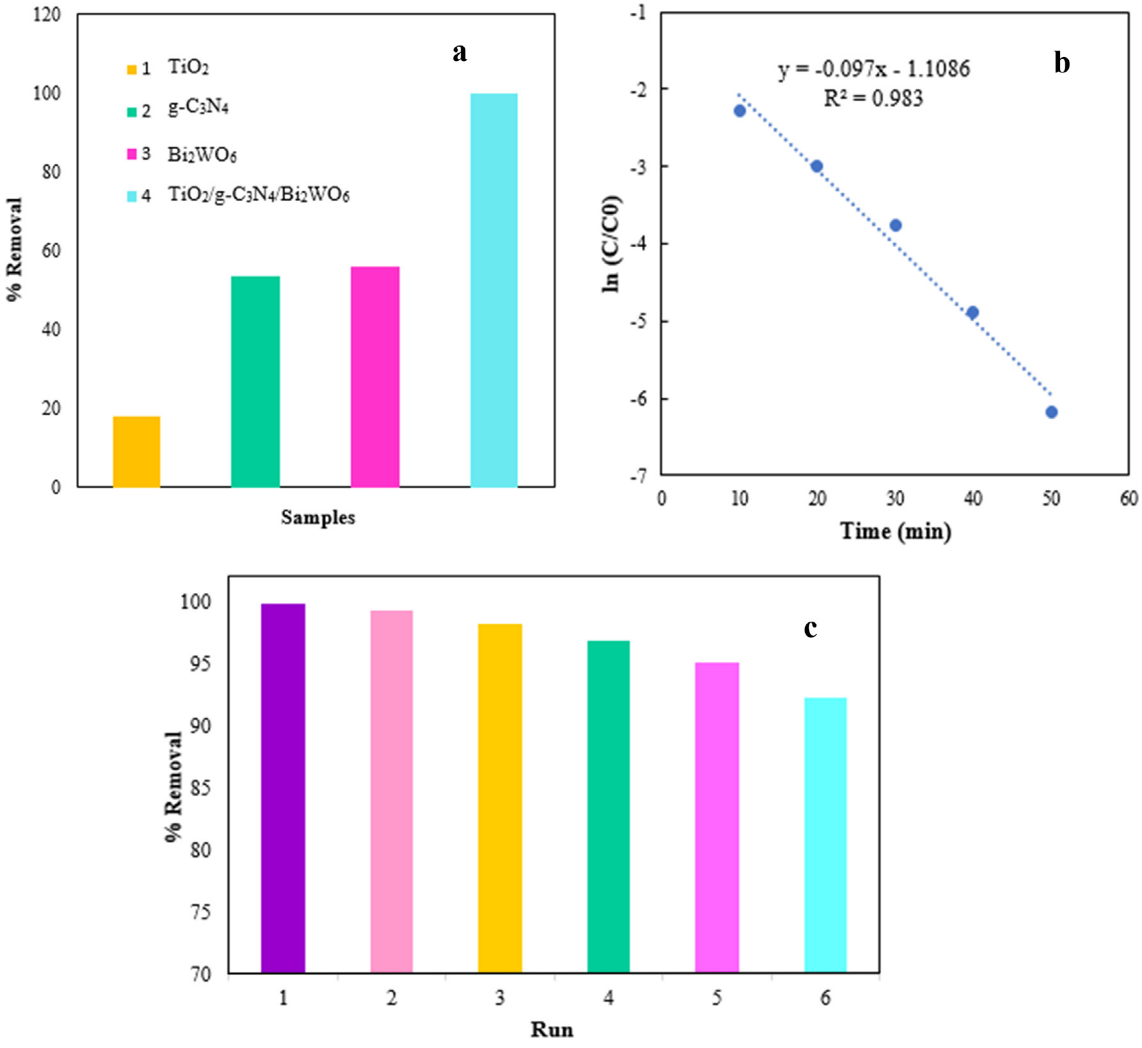

Fig. 7 The comparison of photodegradation activity of as-prepared TiO_2, g-C_3N_4, Bi_2WO_6, and TiO_2/g-C_3N_4/Bi_2WO_6 samples in the optimal conditions (a), photodegradation kinetic over the TiO_2/g-C_3N_4/Bi_2WO_6 nanocomposite (b), and recycling tests for photocatalytic degradation of BG by TiO_2/g-C_3N_4/Bi_2WO_6 nanocomposite (c).

and as a result, greatly increased the photodegradation activity of TiO_2/g-C_3N_4/Bi_2WO_6 nanocomposite. This system with Bi_2WO_6 as electron mediator and g-C_3N_4 as hole traps effectively improved the photo-exited electrons and holes separation, and as a result, greatly enhanced the photodegradation activity of TiO_2.

4. Conclusion

In summary, the novel TiO_2/g-C_3N_4/Bi_2WO_6 ternary heterojunction was successfully synthesized, which was applied as a new photocatalyst for the highly efficient removal of BG dye from aqueous solution. FE-SEM, EDS, mapping, FT-IR, and XRD analyses confirmed the successful synthesis of TiO_2, g-C_3N_4, Bi_2WO_6, and TiO_2/g-C_3N_4/Bi_2WO_6 nanostructures. The optical band gap of TiO_2/g-C_3N_4/Bi_2WO_6 nanocomposite was remarkably reduced from 3.15 eV to 2.68 eV for pure TiO_2 nanoparticles. The significant quenching in the PL spectra and smaller semicircle diameter of the EIS Nyquist plot shown the effective separation of electron and hole pairs and fast charge transfer in the TiO_2/g-C_3N_4/Bi_2WO_6 photocatalyst, respectively. The effects of four key parameters

Table 5 Absolute electronegativity, Band gap energy (E_g), Conduction band and valance band potentials (E_{CB} and E_{VB}) of TiO_2, g-C_3N_4, and Bi_2WO_6 on NHE.

Photocatalyst	χ (eV)	E_g (eV)	E_{CB} (eV)	E_{VB} (eV)
TiO_2	5.81	3.15	−0.265	2.885
g-C_3N_4	4.67	2.68	−1.17	1.51
Bi_2WO_6	6.36	2.96	0.38	3.34

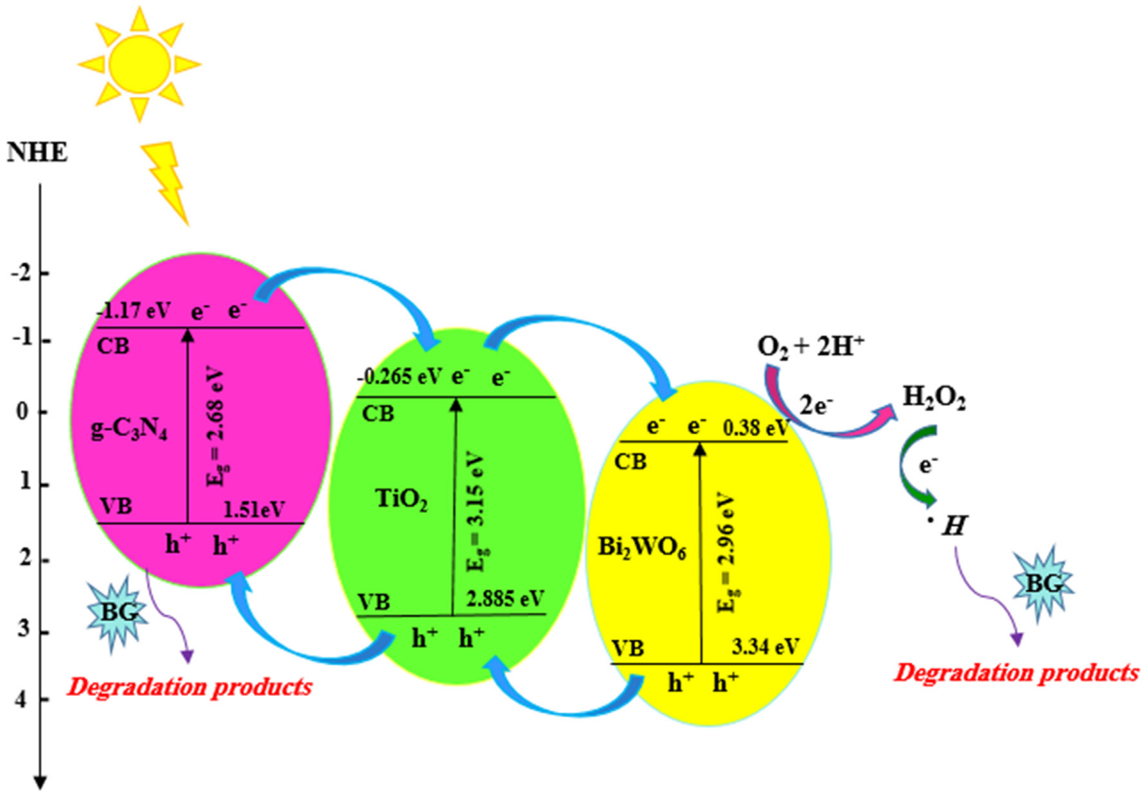

Fig. 8 Proposed BG photodegradation mechanism using TiO_2/g-C_3N_4/Bi_2WO_6 heterojunction under visible light irradiation.

(catalyst dosage, initial BG concentration, irradiation time, and pH) on the degradation process were investigated via 2^{k-1} factorial design. According to the results of ANOVA, these key parameters have a significant influence on the removal of BG dye. Also, the predictability and significantly of the model were confirmed by correlation coefficients value obtained from predicted-R^2 of 0.9921 and adjusted-R^2 of 0.9963. In order to improvement the photocatalytic performance of ternary nanocomposite, RSM optimization was used. In the BG degradation procedure, the experimental value of 99.92 % is in good agreement with RSM-response value of 100 %. Also, the pseudo-first-order kinetic model was used to investigate the kinetic of BG degradation by TiO_2/g-C_3N_4/Bi_2WO_6 nanocomposite. According to the results, the k_{app} value for BG degradation was estimated 0.097 min^{-1}. The TiO_2/g-C_3N_4/Bi_2WO_6 nanocomposite was reused for six cycles without a considerable decrease in the photocatalytic activity, which this capability was confirmed the good stability of this nanocomposite.

Declaration of Competing Interest

The authors declare that they have no known competing financial interests or personal relationships that could have appeared to influence the work reported in this paper.

Acknowledgements

The authors would like to express their sincere appreciation to the founders of Kerman University, Mr Alireza Afzalipour and his wife, Mrs Fakhereh Saba, for their foresight and generosity in training future generations of doctors, engineers and scientists. In addition, the authors would like to acknowledge their thanks to Dr Parviz Dabiri for his generous support for the research activities of the chemistry laboratories in Kerman University.

References

Abdel-Wahed, M.S., El-Kalliny, A.S., Badawy, M.I., Attia, M.S., Gad-Allah, T.A., 2020. Core double-shell $MnFe_2O_4$@rGO@TiO_2 superparamagnetic photocatalyst for wastewater treatment under solar light. Chem. Eng. J. 382, 122936.

Ahmadpour, N., Sayadi, M.H., Homaeigohar, S., 2020. A hierarchical Ca/TiO_2/NH_2-MIL-125 nanocomposite photocatalyst for solar visible light induced photodegradation of organic dye pollutants in water. RSC Adv. 10, 29808–29820.

Baniamerian, H., Tsapekos, P., Morales, M.A., Shokrollahzadeh, S., Safavi, M., Angelidaki, I., 2020. Anti-algal activity of Fe_2O_3–TiO_2 photocatalyst on Chlorella vulgaris species under visible light irradiation. Chemosphere 242, 125119.

Chandra, R., Mukhopadhyay, S., Nath, M., 2016. TiO_2@ZIF-8: A novel approach of modifying micro-environment for enhanced photo-catalytic dye degradation and high usability of TiO_2 nanoparticles. Mater. Lett. 164, 571–574.

Chang, C.-J., Chen, J.-K., Lin, K.-S., Wei, Y.-H., Chao, P.-Y., Huang, C.-Y., 2020. Enhanced visible-light-driven photocatalytic degradation by metal wire-mesh supported Ag/flower-like Bi_2WO_6 photocatalysts. J. Alloys Compd. 813, 152186.

Chen, X., Wang, D., Wang, T., et al, 2019. Enhanced Photoresponsivity of a GaAs Nanowire Metal-Semiconductor-Metal Photodetector by Adjusting the Fermi Level. ACS Appl. Mater. Interfaces. 36, 33188–33193.

Chinnapaiyan, S., Chen, T.-W., Chen, S.-M., Alothman, Z.A., Ali, M. A., Wabaidur, S.M., Al-Hemaid, F., Lee, S.-Y., Chang, W.-H., 2020. Ultrasonic-assisted Preparation and Characterization of

Magnetic $ZnFe_2O_4$/gC_3N_4 Nanomaterial and their Applications towards Electrocatalytic Reduction of 4-Nitrophenol. Ultrason. Sonochem. 68, 105071.

Deng, Y., Zhao, R., 2015. Advanced oxidation processes (AOPs) in wastewater treatment. Curr. Pollut. Rep. 1, 167–176.

Ding, J., Liu, Q., Zhang, Z., Liu, X., Zhao, J., Cheng, S., Zong, B., Dai, W.-L., 2015. Carbon nitride nanosheets decorated with WO_3 nanorouds: Ultrasoniv assisted facial synthesis and catalytic application in the green manufacture of dialdehydes. Appl. Catal B-Environ. 165, 511–518.

Eshaq, G., Wang, S., Sun, H., Sillanpaa, M., 2020. Superior performance of $FeVO_4$@CeO_2 uniform core-shell nanostructures in heterogeneous Fenton-sonophotocatalytic degradation of 4-nitrophenol. J. Hazard. Mater. 382, 121059.

Gao, D., Liu, W., Xu, Y., Wang, P., Fan, J., Yu, H., 2020. Core-shell Ag@Ni cocatalyst on the TiO_2 photocatalyst: One-step photoinduced deposition and its improved H_2-evolution activity. Appl. Catal. B. 260, 118190.

Golshan, M., Kakavandi, B., Ahmadi, M., Azizi, M., 2018. Photocatalytic activation of peroxymonosulfate by TiO2 anchored on cupper ferrite (TiO_2@$CuFe_2O_4$) into 2,4-D degradation: Process feasibility, mechanism and pathway. J. Hazard. Mater. 38359, 325–337.

Guo, W., Kai, F., Jiajun, Z., Chunjian, X., 2018. 2D/2D Z-scheme Bi2WO6/Porous-g-C3N4 with synergy of adsorption and visible-light-driven photodegradation. Appl. Surf. Sci. 447, 125–134.

Guo, Z., Zhao, Q., Zhang, Y., Li, B., Li, L., Feng, L., Wang, M., Meng, X., Zuo, G., 2020. A novel "turn-on" fluorescent sensor for hydrogen peroxide based on oxidized porous g-C_3N_4 nanosheets. J. Biomed. Mater. Res. 108, 1077–1084.

Hafeez, H.Y., Lakhera, S.K., Karthik, P., Anpo, M., Neppolian, B., 2018. Facile construction of ternary $CuFe_2O_4$-TiO_2 Nanocomposite Supported Reduced Graphene Oxide (rGO) photocatalysts for the efficient Hydrogen Production. Appl. Surf. Sci. 449, 772–779.

Hafeez, H.Y., Lakhera, S.K., Narayanan, N., Harish, S., Hayakawa, Y., Lee, B.-K., Neppolian, B., 2019. Environmentally Sustainable Synthesis of a $CoFe_2O_4$-TiO_2/rGO Ternary Photocatalyst: A Highly Efficient and Stable Photocatalyst for High Production of Hydrogen (Solar Fuel). ACS Omega 4, 880–891.

Huang, G., Li, S., Liu, L., Zhu, L., Wang, Q., 2019. Ti_3C_2 MXene-Modified Bi_2WO_6 Nanoplates for Efficient Photodegradation of Volatile Organic Compounds. Appl. Catal. B 244, 974–982.

Huang, M., Yu, J., Hu, Q., Su, W., Fan, M., Li, B., Dong, L., 2016. Preparation and enhanced photocatalytic activity of carbon nitride/titania (001 vs 101 facets)/reduced graphene oxide (g-C_3N_4/TiO_2/rGO) hybrids under visible light. Appl. Surf. Sci. 389, 1084–1093.

Kai, W., Kexin, L., Liushui, Y., Shenglian, L., Huiqin, G., Yuhua, D., Xubiao, L., 2018. One-step fabrication of g-C_3N_4 nanosheets/TiO2 hollow microspheres heterojunctions with atomic level hybridization and their application in the multi-component synergistic photocatalytic systems. Appl. Catal. B. 222, 88–98.

Karthik, P., Kumar, T.R.N., Neppolian, B., 2020. Redox couple mediated charge carrier separation in g-C_3N_4/CuO photocatalyst for enhanced photocatalytic H_2 production. Int. J. Hydrog. Energy 45, 7541–7551.

Khan, Z.U.H., Shah, N.S., Iqbal, J., Khan, A.U., Imran, M., Alshehri, S.M., Muhammad, N., Sayed, M., Ahmad, N., Kousar, A., Ashfaq, M., Howari, F., Tahir, K., 2020. Biomedical and photocatalytic applications of biosynthesized silver nanoparticles: Ecotoxicology study of brilliant green dye and its mechanistic degradation pathways. J. Mol. Liq. 319, 114114.

Koutavarapu, R., Babu, B., Reddy, C.V., Reddy, I.N., Reddy, K.R., Rao, M.C., Aminabhavi, T.M., Cho, M., Kim, D., Shim, J., 2020. ZnO nanosheets-decorated Bi_2WO_6 nanolayers as effcient photocatalysts for the removal of toxic environmental pollutants and photoelectrochemical solar water oxidation. J. Environ. Manage. 265, 110504.

Kovalevskiy, N., Selishchev, D., Svintsitskiy, D., Selishcheva, S., Berezin, A., Kozlov, D., 2020. Synergistic effect of polychromatic radiation on visible light activity of N-doped TiO_2 photocatalyst. Catal. Commun. 134, 105841.

Lakhera, S.K., Vijayarajan, V.S., Krishna, B.S.R., Veluswamy, P., Neppolian, B., 2020. Cobalt phosphate hydroxide loaded g-C_3N_4 photocatalysts and its hydrogen production activity. Int. J. Hydrog. Energy 45, 7562–7573.

Li, R., Cai, M., Xie, Z., Zhang, Q., Zeng, Y., Liu, H., Liu, G., Lv, W., 2020a. Construction of heterostructured $CuFe_2O_4$/g-C_3N_4 nanocomposite as an efficient visible light photocatalyst with peroxydisulfate for the organic oxidation. Appl. Catal. B 244, 974–982.

Li, S., Chen, J., Hu, S., Wang, H., Jiang, W., Chen, X., 2020b. Facile construction of novel Bi_2WO_6/Ta_3N_5 Z-scheme heterojunction nanofibers for efficient degradation of harmful pharmaceutical pollutants. Chem. Eng. J. 402, 126165.

Liu, J., Luo, Z., Han, W., Zhao, Y., Li, P., 2020a. Preparation of ZnO/Bi_2WO_6 heterostructures with improved photocatalytic performance. Mater. Sci. Semicond. Process. 106, 104761.

Liu, S.-H., Tang, W.-T., Chou, P.-H., 2020b. Microwave-assisted synthesis of triple 2D g-C_3N_4/Bi_2WO_6/rGO composites for ibuprofen photodegradation: Kinetics, mechanism and toxicity evaluation of degradation products. Chem. Eng. J. 387, 124096.

Li, Y., Zhang, P., Wan, D., Xue, C., Zhao, J., Shao, G., 2020c. Direct evidence of 2D/1D heterojunction enhancement on photocatalytic activity through assembling MoS_2 nanosheets onto super-long TiO_2 nanofibers. Appl. Surf. Sci. 504, 144361.

Liu, Y., Zhang, Q., Yuan, H., et al, 2021. Comparative study of photocatalysis and gas sensing of ZnO/Ag nanocomposites synthesized by one- and two-step polymer-network gel processes. J. Alloys Compd. 868.

Lopes, F.C.S.M.R., Rocha, M.G.C., Bargiela, P., Ferreira, H.S., Pires, C.A.M., 2020. Ag/TiO_2 photocatalyst immobilized onto modified natural fibers for photodegradation of anthracene. Chem. Eng. Sci. 227, 115939.

Maniakova, G., Kowalska, K., Murgolo, S., Mascolom, G., Libralato, G., Lofrano, G., Sacco, O., Guida, M., Rizzo, L., 2020. Comparison between heterogeneous and homogeneous solar driven advanced oxidation processes for urban wastewater treatment: Pharmaceuticals removal and toxicity. Sep. Purif. Technol. 236, 116249.

Muneer, I., Farrukh, M.A., Ali, D., Bashir, F., 2021. Heterogeneous photocatalytic degradation of organic dyes by highly efficient $GdCoSnO_3$. Mater. Sci. Eng., B. 265, 115028.

Nithya, R., Ragupathy, S., Sakthi, D., Arun, V., Kannadasan, N., 2020. A study on Mn doped ZnO loaded on CSAC for the photocatalytic degradation of brilliant green dye. Chem. Phys. Lett. 755, 137769.

Noda, C., Asakura, Y., Shiraki, K., Yamakata, A., Yin, S., 2020. Synthesis of three-component C_3N_4/rGO/C-TiO_2 photocatalyst with enhanced visible-light responsive photocatalytic deNO_x activity. Chem. Eng. J. 390, 124616.

Ouyang, X., Tang, L., Feng, C., Peng, B., Liu, Y., Ren, X., Zhu, X., Tan, J., Hu, X., 2020. Au/CeO_2/g-C_3N_4 heterostructures: Designing a self-powered aptasensor for ultrasensitive detection of Microcystin-LR by density functional theory. Biosens. Bioelectron. 164, 112328.

Panigrahi, P., Kumar, A., Karton, A., Ahuja, R., Hussain, T., 2020. Remarkable improvement in hydrogen storage capacities of two-dimensional carbon nitride (g-C_3N_4) nanosheets under selected transition metal doping. Int. J. Hydrog. Energy 45, 3035–3045.

Raza, A., Shen, H., Haidry, A.A., Cui, S., 2018. Hydrothermal synthesis of Fe_3O_4/TiO_2/g-C_3N_4: Advanced photocatalytic application. Appl. Surf. Sci. 488, 887–895.

Shakir, K., Elkafrawy, A.F., Ghoneimy, H.F., Beheir, S.G.E., Refaat, M., 2010. Removal of rhodamine B (a basic dye) and thoron (an acidic dye) from dilute aqueous solutions and wastewater simulants by ion flotation. Water Res. 44, 1449–1461.

Shang, M., Wenzhong, W., Ling, Z., Songmei, S., Lu, W., Lin, Z., 2009. 3D Bi_2WO_6/TiO_2 hierarchical heterostructure: controllable synthesis and enhanced visible photocatalytic degradation performances. J. Phys. Chem. C. 113, 14727–14731.

Sharma, A., Liu, N., Ma, Q., Zheng, H., Kawazoe, N., Chen, G., Yang, Y., 2020. PEG assisted P/Ag/Ag_2O/Ag_3PO_4/TiO_2 photocatalyst with enhanced elimination of emerging organic pollutants in salinity condition under solar light illumination. Chem. Eng. J. 385, 123765.

Sun, M., Yao, Y., Ding, W., Anandan, S., 2020. N/Ti^{3+} co-doping biphasic TiO_2/Bi_2WO_6 heterojunctions: Hydrothermal fabrication and sonophotocatalytic degradation of organic pollutants. J. Alloys Compd. 820, 153172.

Tekin, D., Kiziltas, H., Ungan, H., 2020. Kinetic evaluation of ZnO/TiO_2 thin film photocatalyst in photocatalytic degradation of Orange G. J. Mol. Liq. 306, 112906.

Tiana, N., Huang, H., He, Y., Guo, Y., Zhang, T., Zhang, Y., 2015. Mediator-Free Direct Z-scheme Photocatalytic System: $BiVO_4$/g-C_3N_4 OrganicInorganic Hybrid Photocatalyst with Highly Efficient Visible-Light-Induced Photocatalytic Activity. Dalton Trans. 44, 4297–4307.

Vadivel, S., Kamalakannan, P.V., Kavitha, P.N., Santhoshini, T.P., Balasubramanian, N., 2016. Development of novel Ag modified BiOF squares/g-C_3N_4 composite for photocatalytic applications. Mater. Sci. Semicond. Process. 41, 59–66.

Wang, C.-C., Li, J.-R., Lv, X.-L., Zhang, Y.-Q., Guo, G., 2014. Photocatalytic organic pollutants degradation in metal–organic frameworks. Energy Environ. Sci. 7, 2831–2867.

Wang, C.-Y., Zeng, W.-J., Jiang, T.-T., Chen, X., Zhang, X.-L., 2019. Incorporating attapulgite nanorods into graphene oxide nanofiltration membranes for efficient dyes wastewater treatment. Sep. Purif. Technol. 214, 21–30.

Wang, J., Yu, W., Graham, N.J.D., Jiang, L., 2020. Evaluation of a novel polyamide-polyethylenimine nanofiltration membrane for wastewater treatment: Removal of Cu^{2+} ions. Chem. Eng. J. 392, 123769.

Wei, X-N., Wang, H-L., 2018. Preparation of magnetic g-$C_3N_4/Fe_3O_4/TiO_2$ photocatalyst for visible light photocatalytic application. J. Alloys Compd. 763, 844-853

Wu, S., Sun, J., Li, Q., Hood, Z.D., Yang, S., Su, T., Peng, R., Wu, Z., Sun, W., Kent, P.R.C., Jiang, B., Chisholm, M.F., 2020. Effects of Surface Terminations of 2D Bi_2WO_6 on Photocatalytic Hydrogen Evolution from Water Splitting.ACS Appl. Mater. Interfaces 12, 20067–20074.

Yang, P., Wang, J., Yue, G., Yang, R., Zhao, P., Yang, L., Zhao, X., Astruc, D., 2020. Constructing mesoporous g-C_3N_4/ZnO nanosheets catalyst for enhanced visible-light driven photocatalytic activity. J. Photochem. Photobiol. A 388, 112169.

Yin, S., Chen, Y., Gao, C., Hu, Q., Li, M., Ding, Y., Di, J., Xia, J., Li, H., 2020. In-situ preparation of MIL-125(Ti)/Bi_2WO_6 photocatalyst with accelerating charge carriers for the photodegradation of tetracycline hydrochloride. J. Photochem. Photobiol. A 387, 112149.

Yuan, C., Gao, H., Xu, Q., Song, X., Zhai, C., Zhu, M., 2020. Pt decorated 2D/3D heterostructure of Bi_2WO_6 nanosheet/Cu_2S snowflake for improving electrocatalytic methanol oxidation with visible-light assistance. Appl. Surf. Sci. 521, 146431.

Yuan, X.Z., Meng, Y.T., Zeng, G.M., Fang, Y.Y., Shi, J.G., 2008. Evaluation of tea-derived biosurfactant on removing heavy metal ions from dilute wastewater by ion flotation. Colloids Surf. A Physicochem. Eng. Asp. 317, 256–261.

Yu, C., Wei, L., Li, X., Chen, J., Fan, Q., Yu, J.C., 2013. Synthesis and characterization of Ag/TiO_2-B nanosquares with high photocatalytic activity under visible light irradiation. Mater. Sci. Eng B. 178, 344–348.

Zhang, C., Zhou, Y., Bao, J., Fang, J., Zhao, S., Zhang, Y., Sheng, X., Chen, W., 2018. Structure regulation of ZnS@g-C_3N_4/TiO_2 nanospheres for efficient photocatalytic H_2 production under visible-light irradiation. Chem. Eng. J. 346, 226–237.

Zhao, T., Xing, Z., Xiu, Z., Li, Z., Yang, S., Zhu, Q., Zhou, W., 2019. Surface defect and rational design of TiO_{2-x} nanobelts/ g-C_3N_4 nanosheets/ CdS quantum dots hierarchical structure for enhanced visible-light-driven photocatalysis. Int. J. Hydrog. 44, 1586–1596.

Zhang, L., Cong, M., Ding, X., et al, 2020. A Janus Fe-SnO2 Catalyst that Enables Bifunctional Electrochemical Nitrogen Fixation. Angew. Chem. Int. Ed 59, 10980–10985.

Zhang, M., Sun, X., Wang, C., et al, 2022. Photocatalytic degradation of rhodamine B using Bi4O5Br 2-doped ZSM-5. Materials chemistry and physics. Mater. Chem, Phys.

Zheng, L., Jiao, Y., Zhong, H., Zhang, C., Wang, J., Wei, Y., 2020. Insight into the magnetic lime coagulation-membrane distillation process for desulfurization wastewater treatment: From pollutant removal feature to membrane fouling. J. Hazard. Mater. 391, 122202.

Zhou, L., Zhou, H., Yang, X., 2019. Preparation and performance of a novel starch-based inorganic/organic composite coagulant for textile wastewater treatment. Sep. Purif. Technol. 210, 93–99.

Zhu, D., Zhou, Q., 2020. Novel Bi2WO6 Modified by N-Doped Graphitic Carbon Nitride Photocatalyst for Efficient Photocatalytic Degradation of Phenol under Visible Light. Appl. Catal. B 268, 118426.